Modeling Jovian hectometric attenuation lanes during the Cassini flyby of Jupiter

AUTHOR(S):

Imai, Masafumi; Lecacheux, Alain; Moncuquet, Michel; Bagenal, Fran; Higgins, Charles A.; Imai, Kazumasa; Thieman, James R.

CITATION:

Imai, Masafumi ...[et al]. Modeling Jovian hectometric attenuation lanes during the Cassini flyby of Jupiter. Journal of Geophysical Research: Space Physics 2015, 120(3): 1888-1907

ISSUE DATE:

2015-03-19

URL:

http://hdl.handle.net/2433/198676

AGU PUBLICATIONS

JGR

Journal of Geophysical Research: Space Physics

RESEARCH ARTICLE
10.1002/2014JA020815

Key Points:
- We compare attenuation lanes with observations and ray-tracing computations
- The lanes can be due to refraction from enhanced density irregularity
- We incorporate a more realistic model of Jovian inner magnetosphere

Correspondence to:
M. Imai,
imai@kugi.kyoto-u.ac.jp

Citation:
Imai, M., A. Lecacheux, M. Moncuquet, F. Bagenal, C. A. Higgins, K. Imai, and J. R. Thieman (2015), Modeling Jovian hectometric attenuation lanes during the Cassini flyby of Jupiter, *J. Geophys. Res. Space Physics*, *120*, 1888–1907, doi:10.1002/2014JA020815.

Received 10 NOV 2014
Accepted 18 FEB 2015
Accepted article online 22 FEB 2015
Published online 19 MAR 2015

Modeling Jovian hectometric attenuation lanes during the Cassini flyby of Jupiter

Masafumi Imai[1,2], Alain Lecacheux[2], Michel Moncuquet[2], Fran Bagenal[3], Charles A. Higgins[4], Kazumasa Imai[5], and James R. Thieman[6]

[1]Department of Geophysics, Kyoto University, Kyoto, Japan, [2]Laboratoire d'Etudes Spatiales et d'Instrumentation en Astrophysique, CNRS/Observatoire de Paris, Meudon, France, [3]Laboratory for Atmospheric and Space Physics, University of Colorado Boulder, Boulder, Colorado, USA, [4]Department of Physics and Astronomy, Middle Tennessee State University, Murfreesboro, Tennessee, USA, [5]Department of Electrical Engineering and Information Science, Kochi National College of Technology, Kochi, Japan, [6]University of Maryland, Baltimore County, Baltimore, Maryland, USA

Abstract The Jupiter encounter by the Cassini spacecraft in late 2000 and early 2001 unveiled persistent properties of Jupiter's hectometric (HOM) radiation originating along auroral magnetic field lines in the polar regions. One of the unique properties of the HOM dynamic spectrum, known as attenuation lanes, appears as rotationally modulated, well-defined regions of lowered intensity, flanked by regions of enhancement. These lanes seem to be the result of refraction of radio waves in a high-density medium–either caused by Case (i) enhanced density in the magnetic L-shell connected to Io's orbit or Case (ii) in the Io plasma torus itself or both. In this paper, we investigate the HOM ray paths of 0.5–3.0 MHz emissions with various cone half-angles in the continuous radio longitudes generating at the magnetic *L*-value equal to 30. We use bi-kappa particle distributions to derive diffusive equilibrium distributions of density in the Io plasma torus. The enhanced density irregularities along the Io flux shell "ribbon" region can be described with a Gaussian density distribution of a maximum density n_0 and breadth (half-width of the distribution across the flux shell) σ. As a result, we found that the interpretation of Case (i) can be accounted for by the attenuation lanes which appear for all cone half-angles, and the reasonable flux shell density n_0 is, on top of specific latitude-dependent density from the diffusive equilibrium model, estimated as 100 cm^{-3} with the half-width $\sigma = 5.0$ Io radii.

1. Introduction

The second-strongest low-frequency radio emissions in our solar system, after the solar radio bursts, emanate from the Jovian magnetosphere as the consequence of complex interactions between Jupiter's plasma and magnetic field and regularly penetrate into Earth's ionosphere, where the cutoff frequency corresponds to ~10 MHz. Jupiter's nonthermal radio emissions contain five parts, according to the following radiation pattern as detected in dynamic spectra, classified as the decametric (DAM) radio component from a few to 40 MHz, the hectometric (HOM) radio component from 300 kHz to 10 MHz, the broadband kilometric (bKOM) radio component from 10 kHz to 1 MHz, the narrowband kilometric (nKOM) radio component from 100 kHz to 200 kHz, and the quasi-periodic (QP) radio components from 1 to 50 kHz (with an interval of 15 min) and from 1 kHz to 200 kHz (with an interval of 40 min) [cf. *Carr et al.*, 1983; *Clarke et al.*, 2004; *Imai et al.*, 2011a, and references therein]. The four types of radio emissions (DAM, HOM, bKOM, and QP) are considered as auroral radio emissions that emanate at higher latitude above Jovian auroras, while nKOM is believed to escape from localized radio sources within the Io plasma torus. In this study, we focus on the auroral radio emissions, in particular only the HOM component. The auroral radio emissions result from the electron cyclotron maser instability (CMI) [*Wu and Lee*, 1979] in which the unstable populations (such as loss cone and ring-shell particle distributions) of weakly relativistic electrons propagate along auroral magnetic field lines. The nonthermal coherent emissions near the electron gyrofrequency which dominate the right-hand extraordinary (R-X) mode, in turn, escape into space [*Zarka*, 1998; *Treumann*, 2006]. In this section, we briefly describe the general features of the HOM radio emissions and specify the attenuation lanes associated with Jovian HOM emissions.

Since the observations of RAE-1 and IMP-6 spacecraft in the middle 1970s [*Desch and Carr*, 1974; *Brown*, 1974] uncovered the first evidence of Jupiter's HOM radio emissions below the Earth's ionospheric critical

frequency, numerous spacecraft have monitored their persistent radio structures [*Ladreiter and Leblanc*, 1991a; *Zarka*, 1998]. Voyager and Ulysses instruments were able to make separate right- and left-hand (RH and LH) polarization measurements below 1 MHz in the HOM dynamic spectrum [*Ortega-Molina and Lecacheux*, 1991; *Barrow and Lecacheux*, 1995], and this suggested that the RH and LH polarized emissions were extraordinary mode waves coming from northern and southern auroral zones. Since the HOM radiation is thought to be closely related to the auroral brightness [*Gurnett et al.*, 2002], it is widely believed that the HOM radio sources are located along magnetic fields just above the main UV auroral oval [e.g., *Ladreiter and Leblanc*, 1990a; *Menietti et al.*, 2003] (or beyond the L-shell value equal to 7 [*Kurth et al.*, 1997]). However, some studies suggest that the HOM radio sources are inside of the auroral regions such as at the L-shell range of 7–11 [*Ladreiter et al.*, 1994] or 4–6 [*Reiner et al.*, 1993] by means of a direction-finding method using Ulysses Jupiter flyby data.

In terms of terminology, a unique feature of the HOM emissions, called "drifting gaps," was first reported as a rotationally lowered intensity by *Lecacheux et al.* [1980] in the Voyager Jupiter encounter data. After extensively analyzing the same data, *Alexander et al.* [1981] described the gap properties as a function of frequency and central meridian longitude (CML) of Jupiter's System III longitude system, *Green et al.* [1992] and *Higgins et al.* [1995] further examined the dependences on Io phase and magnetic latitude, and all of the above authors classified the features as "lanes." Using data from the Galileo plasma wave instrument, *Gurnett et al.* [1998] labeled them "attenuation bands" and argued that they possess a frequency range of 1 to 3 MHz. However, "band" tends to be used as a span of continuous frequencies at a fixed central frequency, and this is not the case for this phenomenon because of the stripe-like variation in intensity. Also, "drifting gap" includes ambiguity of what "drifting" and "gap" mean, because the former is often used in plasma physics for the motion of particles and the latter implies either frequency width or intensity depth. Therefore, in this paper, we shall briefly refer to these features as attenuation lanes [*Alexander et al.*, 1981; *Green et al.*, 1992; *Higgins et al.*, 1995], which are analogous to modulation lanes associated with Jupiter's DAM radio emissions [*Riihimaa*, 1968].

Observations of attenuation lanes within Jovian HOM radio emissions were made from Voyager 1 and 2, Ulysses, and Cassini spacecraft during their Jupiter encounters and the Galileo spacecraft orbiting around Jupiter, as well as the WIND spacecraft orbiting around Earth [*Lecacheux et al.*, 1980; *Alexander et al.*, 1981; *Green et al.*, 1992; *Gurnett et al.*, 1998; *Higgins et al.*, 1995, 1998, 1999, 2001; *Menietti et al.*, 1999, 2001, 2003; *Imai et al.*, 2011b; *Boudjada et al.*, 2001, 2011]. Some of these are reviewed by *Boudjada et al.* [2011]. The main properties are as follows: (1) the dual lowered intensity within the HOM radiation which is shifted ~90° from each other appears as a (impartial or complete) sinusoidal curve in a frequency versus CML plot [*Higgins et al.*, 1998, 1999], (2) the lowered intensity profiles vary depending upon Jovigraphic (or Jovicentric) latitude of the observer and CML, but the better parameter for investigating the attenuation lanes is magnetic latitude, which approximately contains both functions of the latitude and CML [*Green et al.*, 1992; *Higgins et al.*, 1995; *Boudjada et al.*, 2011; *Imai et al.*, 2011b], (3) enhanced intensity appears on the edges of the attenuation lanes [*Imai et al.*, 2011b], and (4) a positive relationship between attenuation lanes and Io volcanic activity has been reported [*Menietti et al.*, 2001].

In accounting for the attenuation lanes, *Gurnett et al.* [1998] first proposed that they are considered to be a consequence of either coherent scattering or shallow-angle reflection from enhanced density irregularities along the Io L-shell (L-value = 5.9) in the course of radio propagation from the HOM radio sources to an observer. Later, *Menietti et al.* [1999] eliminated the possibility of coherent scattering and asserted instead that the origin of the attenuation lanes was due to near-grazing incidence reflection of the HOM radio emissions passing through enhanced density irregularities along the Io L-shell. Substantial ray-tracing studies of *Higgins et al.* [1999, 2001] supported the opinion of *Menietti et al.* [1999], and *Higgins et al.* [2001] used a model of enhanced density in a magnetic L-shell (centered on L-value = 5.9, an Io diameter wide) with a Gaussian density profile across the flux shell, peaking at a value of 100 cm^{-3}. Another ray-tracing study by *Menietti et al.* [2003] expanded the previous studies and used the model for five selected emission frequencies (1.0, 1.5, 2.0, 2.5, and 3.0 MHz) and two source meridian planes (181.5° and 247° System III longitude). The studies used a Gaussian density distribution across a magnetic flux shell of L-value equal to 5.7 and a "ribbon" region where the cold plasma populations are highest within the Io plasma torus [*Schneider and Trauger*, 1995]. As a result, they concluded that the model reproduces the frequency width of the attenuation lane if one assumes that the enhanced maximum density range is 1–10 cm^{-3} and the density breadth range is 0.088–0.44 R_{Io} (R_{Io} stands for a radius of the moon Io). The density

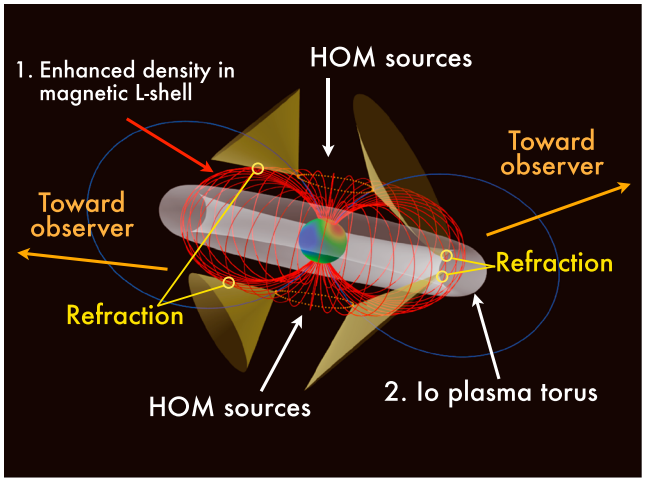

Figure 1. A 3-D computer graphic (CG) image of the geometry of two different proposed models in accounting for Jovian HOM attenuation lanes based on the VIP4 model. The first model was demonstrated by *Gurnett et al.* [1998], and the second was introduced by *Lecacheux* [1981].

breadth is defined as the half-width of the Gaussian density distribution across the magnetic field lines. It is important to note that all previous ray-tracing computations were based not on the enhanced intensity but on the width of the frequency in the intensity of emission for the attenuation lane.

The Io plasma torus plays an important role in affecting the lower frequency of HOM radio emissions. *Lecacheux* [1981] investigated the ray refraction in and near the Io plasma torus by means of ray-tracing technique, suggesting that the rays below 1 MHz are strongly reflected by the simplified, modeled Io plasma torus [*Birmingham et al.*, 1981]. Recently, *Boudjada et al.* [2011] proposed that the attenuation lanes are thought to be the combination of the ray refraction from the Io plasma torus and the frequency-dependent cone half-angle emissions. However, this idea is not tested in the theoretical studies such as the ray-tracing model. The summary of two different models is illustrated in Figure 1.

Recently, *Boudjada et al.* [2011] and *Imai et al.* [2011b] analyzed the attenuation lanes recorded with the Cassini spacecraft during the Jupiter's cruise phase. While *Boudjada et al.* [2011] examined the total intensity of the dynamic spectrum and found that the dual attenuation lanes were intersected in frequency versus magnetic latitude plots, *Imai et al.* [2011b] analyzed the occurrence probability for each HOM polarization and showed that the attenuation lanes clearly have different frequency slopes in the right- and left-hand polarization maps as a function of frequency and magnetic latitude. Also, the latter authors pointed out a higher occurrence probability of the HOM emissions next to the attenuated regions.

In this paper, we extend the analysis of rotationally well-defined lowered intensity and flanked enhancement properties associated with Jovian HOM attenuation lanes by closely examining the initial work of *Imai et al.* [2011b] and perform a comprehensive ray-tracing survey to search for the required quantities (i.e., lowered intensity and flanked enhancement) of the attenuation lanes. In section 2.1, we briefly describe the radio receiver and antenna system on board the Cassini spacecraft, while the polarization analysis method and rotation-based averaging method are adapted for the Cassini data in section 2.2, and their results are presented in section 2.3. The first attempt to incorporate a diffusive equilibrium model of Io plasma torus density into ray-tracing codes are presented in section 3.1. Also, assuming that the HOM radio sources emanate from both northern and southern hemispheres, we survey a range of the reasonable parameters to account for the observed attenuation lanes in sections 3.2 and 3.3. In section 4, we discuss plausible scenarios for producing the attenuation lanes by comparing the Cassini observations with our ray-tracing results. Finally, the conclusions are given in section 5.

2. Cassini Jupiter Observation

The closest approach to Jupiter by the Cassini spacecraft en route to Saturn occurred on 30 December 2000 at a distance of 138 Jovian radii (R_J). We have analyzed HOM emissions from 1 October 2000 to 22 March 2001 during which the Jovigraphic latitude of the spacecraft ranges from +3.7° to −3.7° and the Jovian D_4 magnetic latitude [*Smith et al.*, 1976] from +14.5° to −14.5°. The D_4 model is derived from only the measurements of the Pioneer 11 vector helium magnetometer and is the offset dipole model being suitable for representing the approximation of the magnetic field at large radial distance from Jupiter [*Smith et al.*, 1976]. The main advantage of this model is that it has the largest tilted angle between magnetic and rotational axes among all the dipolar models [*Acuña et al.*, 1983].

2.1. Data Set

The Radio and Plasma Wave Science (RPWS) instrument on the Cassini spacecraft was composed of five onboard receivers that monitored the electric fields from 1 Hz to 16 MHz. The high-frequency receiver (HFR) covers the frequency range from 3.5 kHz to 16 MHz and consists of two sets of four analog receivers with a digital signal processing unit. It is connected to three 10 m long monopole electric field antennas, called here (E_{X_+}, E_{X_-}, E_Z). The E_{X_+} and E_{X_-} antennas can be combined in dipole E_{X_D}. The Cassini RPWS instrument is capable of performing full Stokes polarization measurements and direction-finding, since the HFR computes the complex autocorrelation and cross-correlation (i.e., [$\langle E_X E_X^* \rangle$, $\langle E_X E_Z^* \rangle$, $\langle E_X^* E_Z \rangle$, $\langle E_Z E_Z^* \rangle$], with $X = X_+$, X_-, and X_D) based on the signals received from a pair of antennas either (E_{X_+}, E_Z), (E_{X_-}, E_Z), or (E_{X_D}, E_Z) [*Lecacheux*, 2011]. The E_{X_+} and E_{X_-} monopoles are configured at an angle of 120°, and both are nearly orthogonal to the E_Z monopole. For a full description of the RPWS instrument, see *Gurnett et al.* [2004]. For the present study, only the HF1 band of the HFR was used. The HF1 has a sweep period of 32 s over 76 frequency channels, between 0.325 MHz and 4.075 MHz in 50 kHz steps.

2.2. Polarization and Statistical Analyses

The basic concept of the polarization analysis for the low-frequency radio emissions on a spinning or a three-axis stabilized spacecraft was formulated by *Lecacheux* [1978], and this method was extended to the RPWS instrument on board the Cassini spacecraft [*Lecacheux*, 2011] in the framework of the short antenna approximation. This approximation works up to about 2 MHz when using 10 m antennas on board the Cassini spacecraft. We have applied this technique, which approximately gives the similar antenna response up to 6 MHz from the Cassini wire-grid model [*Rief*, 2013], to the higher frequency of the HOM emissions up to 3 MHz. The wire-grid model can be numerically calibrated to the (complex) effective antenna length vectors for all observed frequencies of Cassini RPWS which are necessary to determine the polarization analysis [*Fischer et al.*, 2001; *Macher*, 2008; *Rief*, 2013].

The way to deduce the polarization response above 2 MHz is based on two main assumptions as follows: (1) the antenna model used is the "equivalent short dipole," which is valid only in the quasi-static approximation for the frequency range below 2 MHz [*Vogl et al.*, 2004]; (2) Jupiter emits only circularly polarized waves (i.e., the linear degree Stokes components $Q = U = 0$), which does a pretty good job for the HOM emissions [*Ortega-Molina and Lecacheux*, 1991] but is not appropriate for the DAM emissions due to observed elliptical polarization [*Carr et al.*, 1983]. Insofar as we work on the above assumptions, the true circular degree Stokes V is calculated by

$$V = V_a \mathrm{sgn}(\cos\theta) / \sqrt{1 - Q_a^2 - U_a^2}, \tag{1}$$

where "sgn" is the sign function, Q_a, U_a, and V_a are the measured ("apparent") polarization, and θ is the source elevation above the antenna plane. Due to the neglected antenna gain variation, total intensity S is proportional to the apparent intensity S_a depending slowly upon observed frequency. Hence, right- and left-hand fluxes S_{RH} and S_{LH} are given by

$$\begin{aligned} S_{\mathrm{RH}} &\approx S(1 - V)/2, \\ S_{\mathrm{LH}} &\approx S(1 + V)/2. \end{aligned} \tag{2}$$

Note that the analyzed data include the two available antenna pairs (E_{X+}, E_Z) and (E_{X-}, E_Z), and we discard the data where the source direction is too close to being within the antenna plane (i.e., so-called an ill-condition $| \pi/2 - \theta | < \pi/4$). Even under these constraints, we have analyzed 357 and 367 Jupiter rotation periods of data for a pair of antennas (E_{X+}, E_Z) and (E_{X-}, E_Z), respectively.

In order to determine the occurrence probability of Jovian HOM radio emissions, we have further utilized the rotation-based averaging method [*Imai et al.*, 2008, 2011a, 2011b], which allows us to reduce any local time effects and long-term variation in data reception as well as minimize the quasi-random background fluctuation influenced by the interference of the spacecraft itself. We normalized the above data of S_{RH} and S_{LH} to the intensity corresponding to 100 R_J distance for each frequency channel. The data are organized by the rotations of Jupiter [cf. *Higgins et al.*, 1999]. Next, we deduce the mean intensity (μ) and standard deviation (σ) for each rotation of Jupiter. In this study, we define the threshold as the mean intensity plus one-fifth standard deviation ($\mu + 0.2\sigma$). An activity count occurs when the radio emission intensity is above the threshold, while an observation count occurs any time the receiver is operating nominally. The

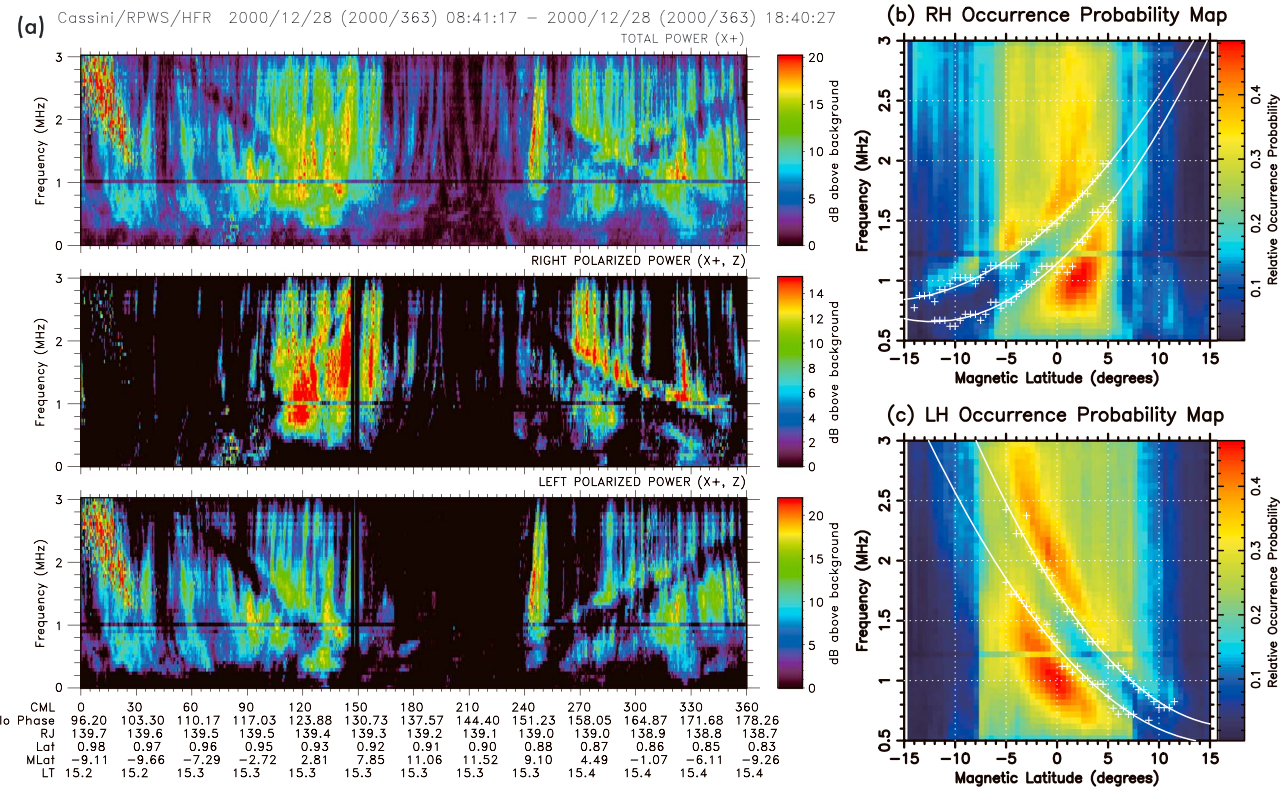

Figure 2. Cassini observations and statistical results. (a) An example of Cassini dynamic spectrum computed with polarization treatment displays the (top) total, (middle) right-polarized, and (bottom) left-polarized power, respectively. The HOM occurrence probability maps of (b) right-hand and (c) left-hand polarization from 0.5 to 3.0 MHz are plotted as a function of Jovian D_4 magnetic latitude [adapted from *Imai et al.*, 2011b]. The white crosses indicate representative points using a central differential method, whereas the white lines are fitted as a quadratic function with a least squares method.

observation and activity counts are sorted into 0.5° bins of Jovian D_4 magnetic latitude but are discarded if their Io phase is in the range of 85°–100° or 235°–260° by taking into account the elimination of the Io-related DAM emissions [*Bigg*, 1964]. This technique allows us to compare the strong and weak emissions with the same weight. The relative occurrence probability is a calculated value between 0 and 1 for each magnetic latitude bin. The value is just the total number of activity counts divided by the total number of observation counts for each bin. The data are recorded by two antenna pairs (E_{X+}, E_Z) and (E_{X-}, E_Z), so the final occurrence probability is given by the total of the occurrence probabilities for each antenna divided by 2, the total available number of antenna pairs in this study. This is done for each frequency.

2.3. Observational Results

We illustrated an example of Jupiter's radio bursts depicted as a function of frequency and CML on 28 December 2000 in Figure 2a. The top, middle, and bottom plots show, respectively, the total and right- and left-polarized powers observed with the HFR receiver of the RPWS instrument. It is obvious that most of the total power is successfully separated into right and left polarization, individually. In particular, the sinusoidal lowered intensity appears in each polarization but is shifted approximately 90° between the two. Another component between 0° and 30° CML classified as Io-related D emissions—which is thought to be coming from southern hemisphere sources and possesses the dominant LH polarization sense—is seen in the DAM radio frequency band. As expected, this emission does not have a pure circular polarization sense due to its elliptical polarization [*Carr et al.*, 1983]. This kind of emission repetitively appears in two particular regions of the Io phase (85°–100° and 235°–260°) [*Bigg*, 1964; *Carr et al.*, 1983], thereby effectively removing it from our statistical HOM study since we said previously that we were excluding emissions in these bands.

Figures 2b and 2c were previously portrayed as the occurrence probability of Jovian HOM radio emissions in frequency versus Jupiter's D_4 magnetic latitude [*Smith et al.*, 1976]. They were briefly reported by *Imai et al.* [2011b]. What is evident is that the high occurrence probability tends to be confined from ~ −7° to ~ +6° of magnetic latitude, and lower probabilities extend into the region between −10° and +10°. This indicates the

Table 1. Values for Fitting the Frequency Widths of Jovian Attenuation Lanes

Polarization	Edge Position	Number of Samples	A	B	C
RH	Upper	39	2.37×10^{-3}	7.98×10^{-2}	1.51
RH	Lower	36	3.22×10^{-3}	7.89×10^{-2}	1.14
LH	Upper	33	3.69×10^{-3}	-1.29×10^{-1}	1.74
LH	Lower	27	3.01×10^{-3}	-9.84×10^{-2}	1.28

HOM averaged radio beaming in latitudinal direction. It is obvious that, as the magnetic latitude increases, the lessened occurrence probability can be seen as the positive frequency slope in Figure 2b and the negative frequency slope in Figure 2c, respectively. This lessened occurrence probability area represents the lowered intensity that we call attenuation lanes. More importantly, it is clear that the attenuation lanes are also combined with an enhancement of the occurrence probability within the HOM emissions at the edges of the lowered intensity region (i.e., the red color in Figures 2b and 2c).

In comparing the ray-tracing results below, it is useful to note the average profile of the frequency widths of the attenuation lanes. To do so, based on the occurrence probability maps in Figures 2b and 2c, we first calculated the derivatives of observed frequency with respect to magnetic latitude by means of the central differential method and normalized all values from 0 to 1. If the values are higher (lower) as frequency increases, they possess a positive (negative) gradient. Second, we extracted a representative point whose value is highest (lowest) in any magnetic latitude on the threshold of above 0.6 (below 0.4) for the upper (lower) edge of the attenuation lanes. Finally, such data are fitted with a quadratic function by means of the least squares method:

$$\mathcal{F} = A \cdot \mathcal{M}^2 + B \cdot \mathcal{M} + C, \tag{3}$$

where $\mathcal{F}$ and $\mathcal{M}$ are, respectively, the observed frequency in MHz and Jovian D_4 magnetic latitude in degrees, and the summary of the best fitting values are given in Table 1. All computed values of the standard deviations are of the order of 10^{-2}, and these errors are very small and do not have much effect on the curves derived above.

3. Ray-Tracing Computations

By using a computer, the first ray-tracing technique formulated by *Haselgrove* [1955] was applied to the whistler mode propagation at the terrestrial magnetosphere in the 1960s [*Yabroff*, 1961; *Kimura*, 1966]. Since then, it has been widely utilized in exploring the propagation effects (refraction, reflection, and evanescence) of ray paths between radio sources and an observer immersed in inhomogeneous anisotropic plasmas and the magnetosphere magnetic field in our solar system. The results are compared with radio observations made from ground stations and spacecraft [*Kimura*, 1997; *Green*, 1988; *Zarka*, 1998]. At Jupiter, this technique has given insight into the investigations of the origins of various aspects of Jupiter's radio emissions such as the bKOM component [*Kimura et al.*, 2008], the HOM component [*Lecacheux*, 1981; *Ladreiter and Leblanc*, 1990a, 1990b, 1991b; *Green et al.*, 1992; *Menietti and Reiner*, 1996; *Higgins et al.*, 1999, 2001, *Menietti et al.*, 2003], and the DAM component [*Hashimoto and Goldstein*, 1983; *Menietti et al.*, 1984a, 1984b; *Green*, 1984]. The effect of plasma density plays an important role in controlling the radio paths of the bKOM and HOM because it is comparable to the effect of magnetic field strength. However, the contribution of plasma density is frequently neglected in the DAM component because the maximum plasma frequency in the Io plasma torus is on the order of ~500 kHz and is small enough to have little effect on the DAM rays, so that the ray trajectories are approximately a straight line from the radio sources to an observer [e.g., *Imai et al.*, 2008, 2011a; *Hess et al.*, 2008, 2010]. In this section, we first express the core of the ray-tracing technique and the conditions for the examination of the attenuation lanes in section 3.1 and then present the results for northern and southern hemisphere radio emissions in sections 3.2 and 3.3, respectively.

3.1. Basics and Initial Conditions

The three-dimensional ray-tracing code in this study was originally developed by *Green* [1984] and *Menietti et al.* [1984a] and applied to investigating the propagation of Jovian HOM emissions by

Table 2. Parameters for Ray-Tracing Computations

	Value and Content
Magnetic field and plasma models	
Magnetic field model	VIP4 model [*Connerney et al.*, 1998] and the washer-shaped current sheet model [*Connerney et al.*, 1981; *Edwards et al.*, 2001]
Plasma model	Combinations of ionosphere model [*Hashimoto and Goldstein*, 1983], diffusive bi-kappa Io plasma torus model [*Moncuquet et al.*, 2002], Jovian global plasma model [*Divine and Garrett*, 1983] with updated equatorial plasma density [*Bagenal and Delamere*, 2011], and magnetic flux shell density model [e.g., *Menietti et al.*, 2003; *Fung and Green*, 2005]
Fixed parameters	
Wave mode	R-X mode
Emission frequencies, f	0.5–3.0 MHz consisting of 26 channels in a 0.1 MHz interval
Radio source distributions	Continuous longitudes from 0 to 350° with a 10° step
Magnetic L-value of source	30 corresponding to feet of the averaged main oval [e.g., *Vogt et al.*, 2011]
f/f_{RX}	1.01
Position of observer	Jovicentric latitude from −3.7° to +3.7° at a fixed 100 R_J distance
Bi-kappa Io plasma torus model parameters	
Kappa parameter, κ	2.4 for electrons and 2 for ions [cf. *Moncuquet et al.*, 2002]
Thermal anisotropy, $T_\perp/T_\parallel$	1.2 for electrons and 3 for ions [cf. *Moncuquet et al.*, 2002]
Free parameters	
Cone half-angle, β	40°–90° for northern hemisphere radio emission and 90°–130° for southern hemisphere radio emission
Magnetic flux shell model parameters	
Maximum density, n_0	1.0–200 cm^{-3}
Breadth of density, σ	0.5–5.0 R_{Io}

Green et al. [1992], *Higgins et al.* [1999, 2001], and *Menietti et al.* [2003]. The essential computation in this code deals with the set of first-order differential equations for determining ray trajectories which were first proposed by *Haselgrove* [1955] in the framework of geometric optical approximation (or WKB approximation) [*Budden*, 1985]. The numeral integration algorithm uses Hamming's predictor-corrector method with a Newton's interpolation plus a Runge-Kutta starter [cf. *Ralston*, 1960]. The calculations of refractive index are based on the cold plasma theory [*Stix*, 1992]. According to the CMI theory demanded for the HOM emissions, the radiation of R-X mode is dominant and its wave cutoff is $f_{RX} = f_g/2 + \sqrt{(f_g/2)^2 + f_p^2}$, where f_p and f_g are the electron plasma frequency and gyrofrequency, respectively.

The necessary input parameters in the initial process of ray-tracing computations are an initial position of the radio source region along a magnetic field line, the emission frequency, the propagation mode (i.e., only R-X mode in this study), and the initial cone half-angle, defined as an angle between the wave vector and the local magnetic field vector. Note that, because the magnetic field vector is outward from the planet in the northern hemisphere and directed into the planet in the southern hemisphere at Jupiter and shows an outward pointing emission cone from Jupiter near both polar regions, the cone half-angle represents an acute angle for northern hemisphere radio emissions and an obtuse angle for southern hemisphere radio emissions. In this study, the discretely launched rays from a given radio source amount to 36 rays with 10° step between them forming the thin-walled hollow-cone beam for each cone half-angle [*Dulk*, 1967]. The parameters of this study are listed in Table 2. In the CMI theory, it is predicted that the initial wave growth rate of R-X mode has a peak with the cone half-angle being approximately 90° [*Wu and Lee*, 1979; *Zarka*, 1998; *Treumann*, 2006]. After the radio generation, it is believed that the emission immediately refracts due

Table 3. Coordinate System for D_4 and VIP4 Dipole With Tilt Angle Between Rotational and Centrifugal Equators

	D_4[a]	VIP4 dipole[b]
Magnetic tilt colatitude	10.8°	9.5°
Centrifugal tilt colatitude	-	6.3°
West longitude	200.8°	200.8°
Meridian plane	-	290.8°
Offset center position[c]	Yes	No

[a]The values are extracted from Table 1.3 of *Acuña et al.* [1983].
[b]The values are computed with VIP4 first-order Gaussian factors [*Connerney et al.*, 1998] from equation (12) in section 18 of *Chapman and Bartels* [1940].
[c]This is a question of whether the rotational center coincides with the magnetic center.

to the surrounding local plasma density around the radio sources. It then propagates more directly toward a distant observer away from Jupiter. Therefore, the value of the cone half-angle contains the combined effects of theoretical prediction and ray refraction near the radio source.

In terms of Jovian magnetic field models used in this study, we have employed a combination of the VIP4 inner magnetic field model [*Connerney et al.*, 1998] and the washer-shaped current sheet model [*Connerney et al.*, 1981] with analytical forms [*Edwards et al.*, 2001]. We call this combination VIP4-CS hereafter. Other combinations of magnetic field models such as the recently developed VIPAL inner magnetic field model [*Hess et al.*, 2011] and the wrap-shaped current sheet model based on Euler potentials [*Khurana*, 1997; *Khurana and Schwarzl*, 2005] with an additional contribution of the magnetic interaction between the solar wind and the magnetosphere [*Engle*, 1991, 1992; *Alexeev and Belenkaya*, 2005] are applicable. However, they are too constrained to reproduce a symmetrical Jovian plasma model in this study (see below). Therefore, a simple but moderate set of magnetic fields is necessary, especially for the reproduction of the diffusive equilibrium model for the Io plasma torus.

The plasma models are linear combinations of the ionosphere model [*Hashimoto and Goldstein*, 1983], the diffusive Io plasma torus model based on bi-kappa particle distributions [*Moncuquet et al.*, 2002], another background plasma (i.e., plasmasphere, inner disc, and outer disc) model [*Divine and Garrett*, 1983] with updated equatorial plasma density (equation (1) and Table 1 in the work of *Bagenal and Delamere* [2011]), and a magnetic flux shell density model [e.g., *Menietti et al.*, 2003; *Fung and Green*, 2005]. One new approach is to incorporate the diffusive equilibrium model for the Io plasma torus instead of the conventional analytical model [*Divine and Garrett*, 1983] because, in this region, it is required to treat plasma as moving along magnetic flux tubes and to let the plasmas be equilibrated with attractive potentials composed of gravity, centrifugal, and mirror force potentials and an ambipolar electric potential [cf. *Thomas et al.*, 2004]. This kind of two-dimensional, symmetrical Io plasma torus model was first computed by *Bagenal* [1994], who collected plasma density and temperature deduced from the data of Voyager 1 and assumed anisotropic hot ions and other isotropic plasmas having the bi-Maxwellian distributions. However, because this model predicted that their functions are proportional to the observer latitude, it cannot explain the observational fact that, as Ulysses traversed from lower to higher latitudes from Jupiter, the increase in electron temperature and the decrease in its density were recorded. In order to overcome this problem, *Moncuquet et al.* [2002] expanded the *Bagenal* [1994] model by assuming plasmas as bi-kappa distributions. In this study, we have used the bi-kappa Io plasma torus model of *Moncuquet et al.* [2002] which assumes the VIP4-CS model.

Prior to ray-tracing computations, we calculated density for electrons and eight ion species (H^+, S^+, S^{++}, S^{+++}, O^+, O^{++}, Na^+, and SO_2^+) along a magnetic field line by solving a set of diffusive equilibrium formulae [*Moncuquet et al.*, 2002, equations (A1)–(A4)]. We then assigned the electron density into a grid of 0.01 R_J and 0.2° latitude in the range of 1 to 13 R_J and of −80° to +80° latitude in the centrifugal coordinate system, which is tilted by about one third of the angle between the spin and the magnetic axes [*Hill et al.*, 1974; *Cummings et al.*, 1980]. All calculations were made in the meridian plane of 290.8° System III longitude, where centrifugal, magnetic, and spin equators are aligned in the VIP4 dipole model (defined in Table 3). The required spatial derivatives for ray tracing are calculated with the centered differential method and then interpolated at any position by the weight-distribution method [*Birdsall and Langdon*, 2005].

To investigate the effects of enhanced density in a magnetic flux shell on Jovian attenuation lanes, an additional flux shell density is incorporated. The total electron density inside a magnetic flux shell model

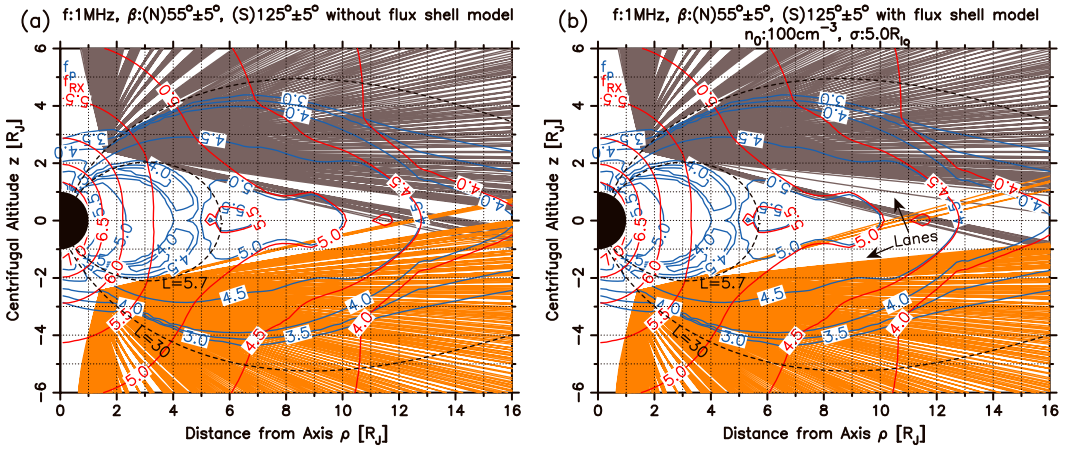

Figure 3. A family of ray paths for emission frequency 1 MHz using the basic combined Jovian plasma models (a) excluding and (b) including the flux shell model. As the values are shown in logarithmical scale in hertz, the red lines are surfaces of R-X cutoff frequency f_{RX} and the blue lines are surfaces of electron plasma frequency f_p. The large vacant radio regions appear more clearly in Figure 3b rather than Figure 3a and are related to the frequency widths of Jovian HOM attenuation lanes.

[e.g., *Menietti et al.*, 2003; *Fung and Green*, 2005] is described as

$$n_e\left(r_{cen},\theta_{cen}\right) = n_{DE} + n_0 \exp\left[-\left(\frac{r_{cen} - r_{fln}\left(\theta_{cen}\right)}{\sigma}\right)^2\right], \quad (4)$$

where n_{DE} in cm^{-3} is the diffusive equilibrium model density, n_0 in cm^{-3} is a maximum density on the central magnetic flux shell, σ in R_{Io} units (where R_{Io} =1820 km is a radius of the moon Io) is the breadth of the flux shell density, r_{fln} in kilometers is the radial distance of a VIP4-CS magnetic field line along L-value = 5.7 (i.e., it penetrates into the ribbon region in the Io plasma torus [*Schneider and Trauger*, 1995]), and r_{cen} and θ_{cen} are radius and latitude in the centrifugal VIP4 dipole coordinate at Jupiter, which is defined in Table 3. Furthermore, r_{fln} is linearly interpolated as the data point tabulated from VIP4-CS model with a 0.1° latitudinal angular length.

In this study, a total of 36 cases are examined with all combinations of six values of flux shell density n_0 [1.0, 10, 50, 100, 150, 200] cm^{-3} and six values of flux shell breadth σ [0.1, 0.2, 0.5, 1.0, 2.0, 5.0] R_{Io}. For each combination, hundreds of thousands to millions of rays are computed depending upon the number of intervals of the cone half-angle used.

3.2. Northern Hemisphere Radio Emission

Figure 3 shows a comparison of ray trajectories for a frequency of emission of 1 MHz when the model (a) excludes and (b) includes the magnetic flux shell density model. Here the radio source is located at the System III longitude of 290°, and the cone half-angle varies from 50° to 60° for northern hemisphere radio emissions. The blue and red contours show the logarithmic scale of the local plasma frequency in hertz and R-X cutoff frequency in hertz, respectively. This plot is sorted in the centrifugal VIP4 dipole coordinate system. It is important to note that, although the magnetic flux shell density model is not added in Figure 3a, a glimpse of the frequency width of the northern attenuation lane appears. The reason is that the diffusive equilibrium model [*Moncuquet et al.*, 2002] gives the amount of 60 cm^{-3} (80 cm^{-3}) at 3 R_J (4 R_J) for both hemispheres along an L-value = 5.7 magnetic field line, where it penetrates into the highest cold density region called the ribbon region. If we further add the flux shell density n_0 = 100 cm^{-3} and its breadth σ = 5.0 R_{Io}, the frequency width of the attenuation lane increases, as seen in Figure 3b.

After computing all rays originating from continuous radio sources (i.e., all longitudes from 0° to 350°), we have plotted the contour of the total ray numbers as a function of frequency and Jovian D_4 magnetic latitude in Figure 4 for a cone half-angle of (a) 55° and of (b) 75° with the beam width of 2°. The grid of data is organized into intervals of 1° magnetic latitude and 0.1 MHz frequency. The white curves represent fits to the observational RH attenuation lane based on equation (3) and Table 1. For both cases, we have confirmed

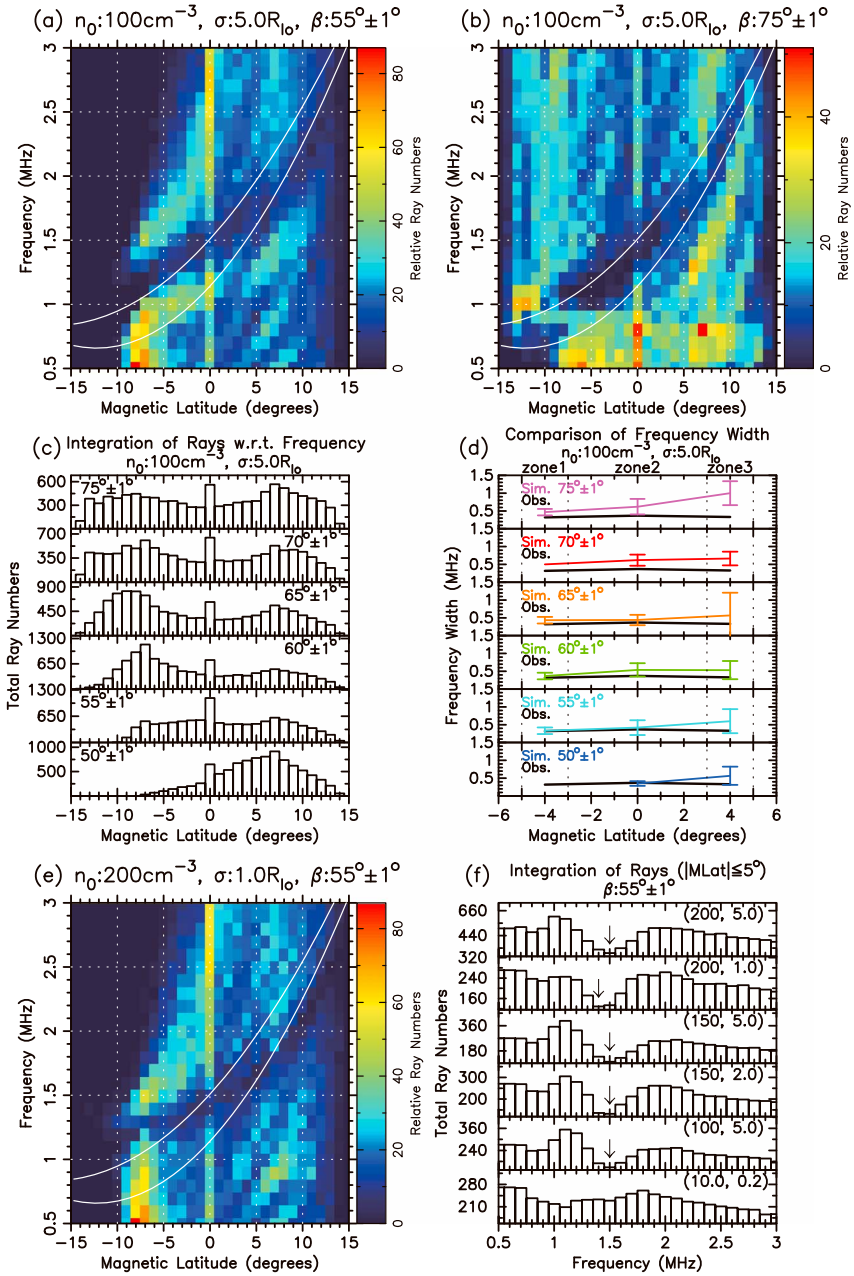

Figure 4. For northern hemisphere radio emission, a number of rays organized in Jovian D_4 magnetic latitude and emission frequency for various cone half-angle and magnetic flux shell parameters. Contours of total number of rays are plotted as a function of frequency and magnetic latitude in the cases of (a) 55° and (b) 75° cone half-angles β with the beam width of 2°, when flux shell density and breadth are respectively fixed with 100 cm^{-3} and 5.0 R_{Io}. (c) Integration of ray numbers with respect to emission frequency are shown from $\beta = 50°$ to 75° with the 2° beam width. (d) Comparison of frequency width of computed attenuation lane is also measured and sorted. The error bars are defined as $\pm t_{90} s/\sqrt{N}$, where t_{90} is a 90% confidence of a t distribution, s is the standard deviation, and N is the sample size. (e) Contours of total ray numbers are sorted in frequency and magnetic latitude for maximum density $n_0 = 200$ cm^{-3} and breadth $\sigma = 1.0$ R_{Io}. (f) When the fixed cone half-angle 55° ± 1° is concerned, the histogram of integration of rays from −5° to +5° magnetic latitude is depicted for the six cases of different flux shell density parameters. The first value inside the parentheses indicates the maximum density of the flux shell, whereas the second shows the breadth of the density.

that the feature of lower ray numbers (related to lower received emission) of the northern attenuation lane is apparent. However, as seen in Figure 4b, the cone half-angle of 75° data gives a much better fit to the observed RH attenuation lanes as far as the lower number of rays shown as the northern attenuation lane compare with the allowable range of the white curves of the RH attenuation lanes.

To examine the trend of anisotropic HOM beaming, we have integrated the total ray numbers with respect to emission frequencies from 0.5 to 3 MHz and then depicted Figure 4c as a function of magnetic latitude. In this histogram, as the emitted cone half-angle varies from 50° to 65° with the 2° beam width, the single broad peak of the total ray numbers gradually moves from +7° to −9° magnetic latitude. Then, the peak seems to be smeared with other peaks above 70° cone half-angle. It is important to note that the spike at 0° magnetic latitude can be seen in all cases because this indicates the edge of the emission cones from all longitudes and this region in turn accumulates the largest amount of rays. As compared with the dominant RH HOM beaming between −7° and +6° magnetic latitude in Figure 2b, our ray-tracing computations in Figure 4c suggest that the northern HOM beaming tends to be confined within cone half-angles of 50° to 60°, whose rays accumulate in the range of magnetic latitude from −7° to +7°.

Furthermore, we have measured the frequency width of the northern attenuation lane and displayed the measurements in Figure 4d. The points to evaluate the frequency widths are defined in section 2.3, but the threshold is optimized for each case. We have divided the main regions clearly showing the attenuation lane by three zones (1) from −5° to −3°, (2) from −3° to +3°, and from (3) +3° to +5° in magnetic latitude, hereafter. The values computed for these zones are plotted at values of −4°, 0°, and +4° for the magnetic latitude, respectively. We have then computed the averages and standard deviations s for each zone. Because of the small sample size and limited ray-tracing computations, we use a 90% confidence of a t distribution t_{90}, and the error bars are calculated as $\pm t_{90} s/\sqrt{N}$, where sample size is N. These computed values are plotted as lines of various colors depending on the cone half-angle cases, and the observational values are also seen as black lines. It is noticed that the cone half-angle 55° ± 1° in zone 1 is not produced because of the outside of HOM beaming shown in the bottom of Figure 4c. Taking into account the allowed error bars in the cone half-angle from 50° to 75°, we have found that the cone half-angles of 55° ± 1° to 60° ± 1° are satisfied with the observational line in all zones. Therefore, the frequency width of the northern attenuation lane reproduced by the ray-tracing computations at the cone half-angles from 55° ± 1° to 60° ± 1° are in good agreement with that measured from the statistical Cassini observation in Figure 2a.

In order to examine the other free parameters of the magnetic flux shell model density, we have considered the variation of the parameters such as maximum density n_0 and density breadth σ, (n_0, σ), for the fixed cone half-angle equal to 55° ± 1°. Two contours are shown in Figure 4a for (100, 5.0) and Figure 4e for (200, 1.0). When comparing them, we recognized that both cases show the frequency width of the northern attenuation lane but the enhancement of the lower edge of the attenuation lane in Figure 4a is larger in ray numbers than in Figure 4e. In terms of the frequency width depending on the magnetic flux shell model parameters, we have integrated the ray numbers with respect to magnetic latitude between −5° and +5° and made the histogram of Figure 4f. From this histogram, the total ray numbers are relatively small near the frequency ~1.5 MHz, where the minima are shown as arrows. This is the evidence of the frequency width within the attenuation lane. In the case of the small values of density and breadth (10.0, 0.2), which is the suggested range of the best fitted parameters given by *Menietti et al.* [2003], there is no clear decrease in ray numbers, and thereby the attenuation lane is not shown.

Just as we considered the HOM beaming and the frequency width of the northern attenuation lane in a thin cone half-angle (with the 2° beam width) above, we now present the results of the thicker cone (with the 10° beam width) for the northern attenuation lane. If we fixed the magnetic flux shell model parameters at a maximum density $n_0 = 100$ cm^{-3} and breadth $\sigma = 5.0\ R_{Io}$, a comparison of the cone half-angle $\beta = 55° \pm 5°$ in Figure 5a and $\beta = 75° \pm 5°$ in Figure 5b shows the similar frequency width but different frequency slope within the attenuation lane, as compared to Figures 4a and 4b. Concerning the frequency slope from the ray-tracing computation, Figure 5b is reasonably consistent with the observational white curves, but the HOM beaming in Figure 5b is wider in magnetic latitude than that in Figure 5a.

Figures 5a and 5b show an enhancement of emission on either side of the attenuation lane (the yellow and red colors). In order to qualitatively discuss these enhancements in Figure 5c, we defined an enhanced rate as maximum of total rays R_{max} divided by normal (background) total rays R_{nom}. In the case of the observation, we adapted two different R_{nom} as the average of the values (1) between −10° and +10°, and (2)

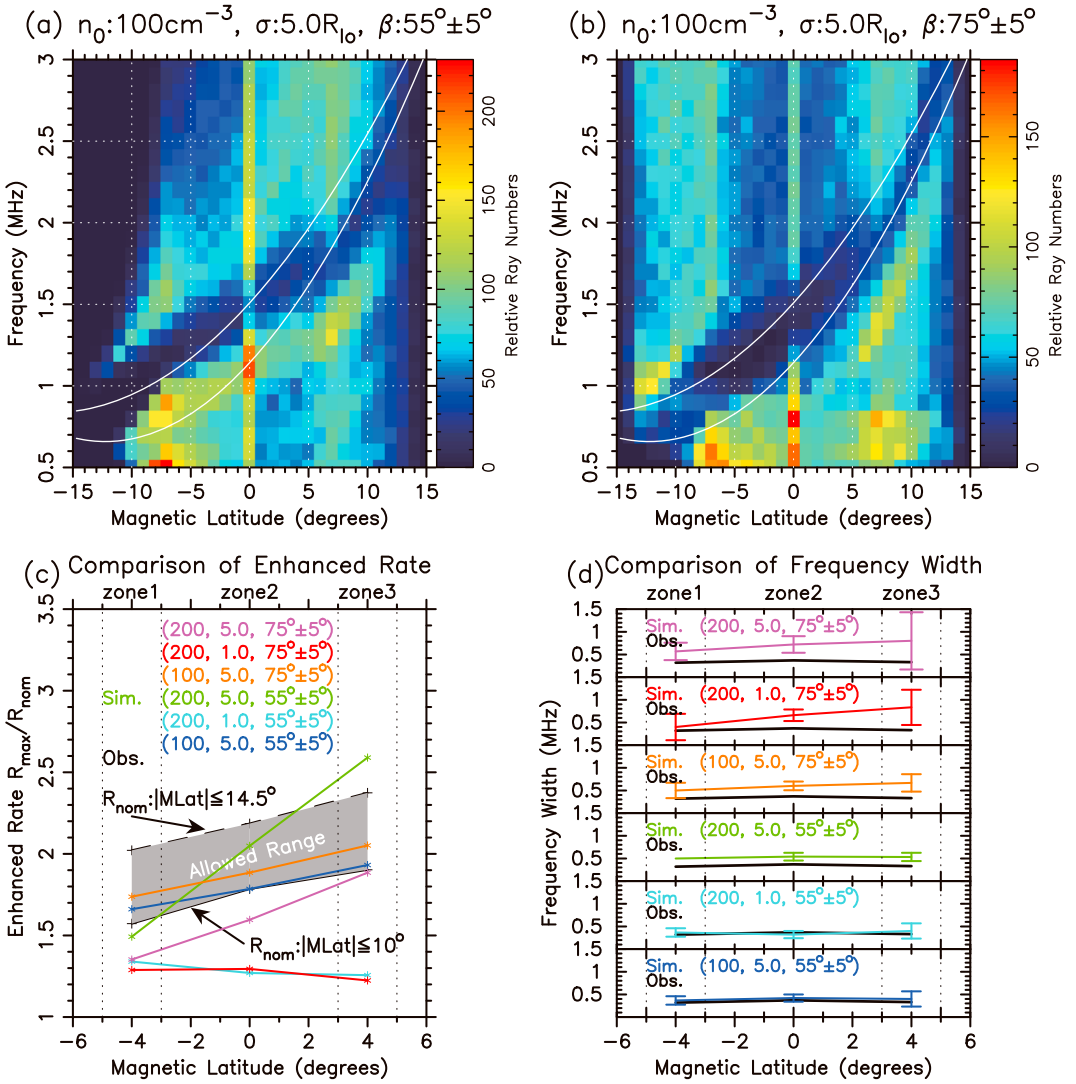

Figure 5. For northern hemisphere radio emission, a number of rays sorted on the functions of magnetic flux shell density parameters and the cone half-angles with the beam width of 10°. Contours of total ray numbers are plotted as a function of frequency and magnetic latitude in the case of maximum density 100 cm^{-3} and breadth 5.0 R_{Io} when the thicker cone half-angles vary for (a) 55°±5° and (b) 75°±5°. (c) The averaged profile of enhanced rate for the observation and six different cases is depicted in magnetic latitude. Each case is labeled as (maximum density, breadth of density, cone half-angle). For the observation profile, two different background quantities R_{nom} are defined as the average values of −14.5° to +14.5° and of −10° to +10°, while those of the calculations are based on the values of no magnetic flux shell density model. (d) Frequency width of the computed attenuation lane is compared with the observation and the six cases. The error bars are again computed as $\pm t_{90}s/\sqrt{N}$.

between −14.5° and +14.5°. The averaged lines for the two cases are similar, but the enhanced rate of case (2) is higher than that of case (1) because R_{nom} of case (1) is lower than that of case (2). By contrast, in the ray-tracing computations, R_{nom} is based on the total ray numbers in the case of no flux shell model. In this study, we defined the allowed range of observations between the lower limit of case (1) and the upper limit of case (2), seen as the gray-colored area in Figure 5c, and then checked if a ray-tracing computation is matched in this range. As a result, in the case of $n_0 = 100$ cm^{-3} and $\sigma = 5.0\,R_{Io}$, the enhanced rates for the cone half-angle $\beta = 55° \pm 5°$ (blue-colored line) and $\beta = 75° \pm 5°$ (orange-colored line) are good enough to meet the above criterion in Figure 5c. The enhanced rates in the case of $n_0 = 200$ cm^{-3} and $\sigma = 1.0\,R_{Io}$ are very small, and the other case (200, 5.0) shows the higher enhanced rates. Nevertheless, the enhanced rates of (100, 5.0) for both the cone half-angle 55° ± 5° and 75° ± 5° clearly agree with the observational allowed range.

In Figure 5d, we have further examined the frequency width of the northern attenuation lane when we choose the six different cases which change the three free parameters (maximum density of flux shell, its breadth, and cone half-angle). This plot has the same format as that of Figure 4d. It is clear that the bottom two graphs, cases of (200, 1.0, 55° ± 5°) and of (100, 5.0, 55° ± 5°), respectively, do reasonably well in accounting for the observational line. For this reason, the reproduction of the frequency width of the attenuation lane is best when the magnetic flux shell density is 100–200 cm^{-3} with a breadth of 1.0–5.0 R_{Io}.

3.3. Southern Hemisphere Radio Emission

Once again, Figure 3 compares ray trajectories for an emission frequency of 1 MHz when the model (a) excludes and (b) includes the magnetic flux shell density model. The cone half-angle for southern hemisphere radio emission varies from 120° to 130°. It is evident that the frequency width of the southern attenuation lane, overall, appears for both cases, but Figure 3b has a wider radio vacant region than Figure 3a. In this section, we investigate the dependence of emitted cone half-angle and magnetic flux shell model parameters such as the maximum density and breadth for the southern attenuation lane.

Similar to the northern hemisphere radio emission, in the case of maximum density $n_0 = 100\ cm^{-3}$ and breadth $\sigma = 5.0\ R_{Io}$, the total number of rays is plotted as a function of frequency and Jovian D_4 magnetic latitude in Figure 6a for the cone half-angle $\beta = 125°$ with the beam width of 2° and Figure 6b for $\beta = 105°$ with the beam width of 2°, respectively. It is worthwhile noting that the cone half-angles 125° and 105° are the complementary angles to the 55° and 75° values used in the northern hemisphere case. Comparing the two cases above with the observational white curves, it is obvious that the positions of the frequency width within the attenuation lane of Figure 6a especially at magnetic latitude from 0° to 10° are higher in frequency than the curves, whereas those of Figure 6b seem to be nearly on the curves.

In integrating the total rays with respect to frequency, Figure 6c shows the location of a single broad peak of total ray numbers that varies from −7° to +10° magnetic latitude when the cone half-angle changes from 130° down to 115°. The broad single peak is somewhat smeared, and there are two broad peaks at the cone half-angle 110°. In addition to the broad peaks, there is always the center spike at 0° magnetic latitude due to the fact that the edge of emission cones from all radio sources focus on this region. In comparison with the LH HOM beaming in Figure 2c, our ray-tracing computations suggest that the southern HOM beaming is confined within cone half-angle from 130° down to 120° because their rays concentrate in the range of magnetic latitude from −7° to +7°.

Furthermore, comparing the frequency width of the southern attenuation lane for cone half-angle dependence in Figure 6d, we divided the major region where attenuation lanes appear into three zones in the same manner of the northern hemisphere radio emission as (1) from −5° to −3°, (2) from −3° to +3°, and (3) from +3° to +5°. We then measured the frequency width of the attenuation lane, as defined in section 3.2. Judging by the error bars, the ray-tracing simulations are in agreement with the observational lines, and we found that all emitted cone half-angles satisfy the expectations. For this reason, in the case of maximum density 100 cm^{-3} and breadth 5.0R_{Io}, the emitted cone half-angle with the beam width of 2°is less sensitive to the frequency width of the southern attenuation lane.

As with the northern case, it is interesting to investigate the dependence of magnetic flux shell model parameters (maximum density n_0, density breadth σ). We have selected the six cases of [(10.0, 0.2), (100, 5.0), (150, 2.0), (150, 5.0), (200, 1.0), (200, 5.0)] using a fixed cone half-angle of 125° with the beaming width of 2°. In choosing the case of (100, 5.0) in Figure 6a and of (200, 1.0) in Figure 6e, the contours of total ray numbers are plotted as a function of emission frequency and magnetic latitude. The appearance of the southern attenuation lane is similar for both cases, but the lower edge of the attenuation lanes in Figure 6a is higher in total number of rays than that in Figure 6e. In expanding to all cases for the existence of southern attenuation lanes, we made the histogram of total rays integrated from −5° to +5° in Figure 6f for the above six cases. Consequently, the frequency 1.7 MHz shows a decrease in the number of rays, and the high peak of rays appears at ∼1.2 MHz, except for (10.0, 0.2), which corresponds to the lowered intensity and flanked enhancement within the attenuation lanes. Therefore, using the exact same argument made in section 3.2 , the case of (10.0, 0.2) does not, again, have enough density to produce those features.

Finally, in examining the thicker HOM beaming cone, we have replotted the total ray numbers as a function of frequency and magnetic latitude in Figures 7a and 7b. It is evident that the enhancement around the lowered intensity of the attenuation lanes is more clearly seen in Figure 7a when we compare with

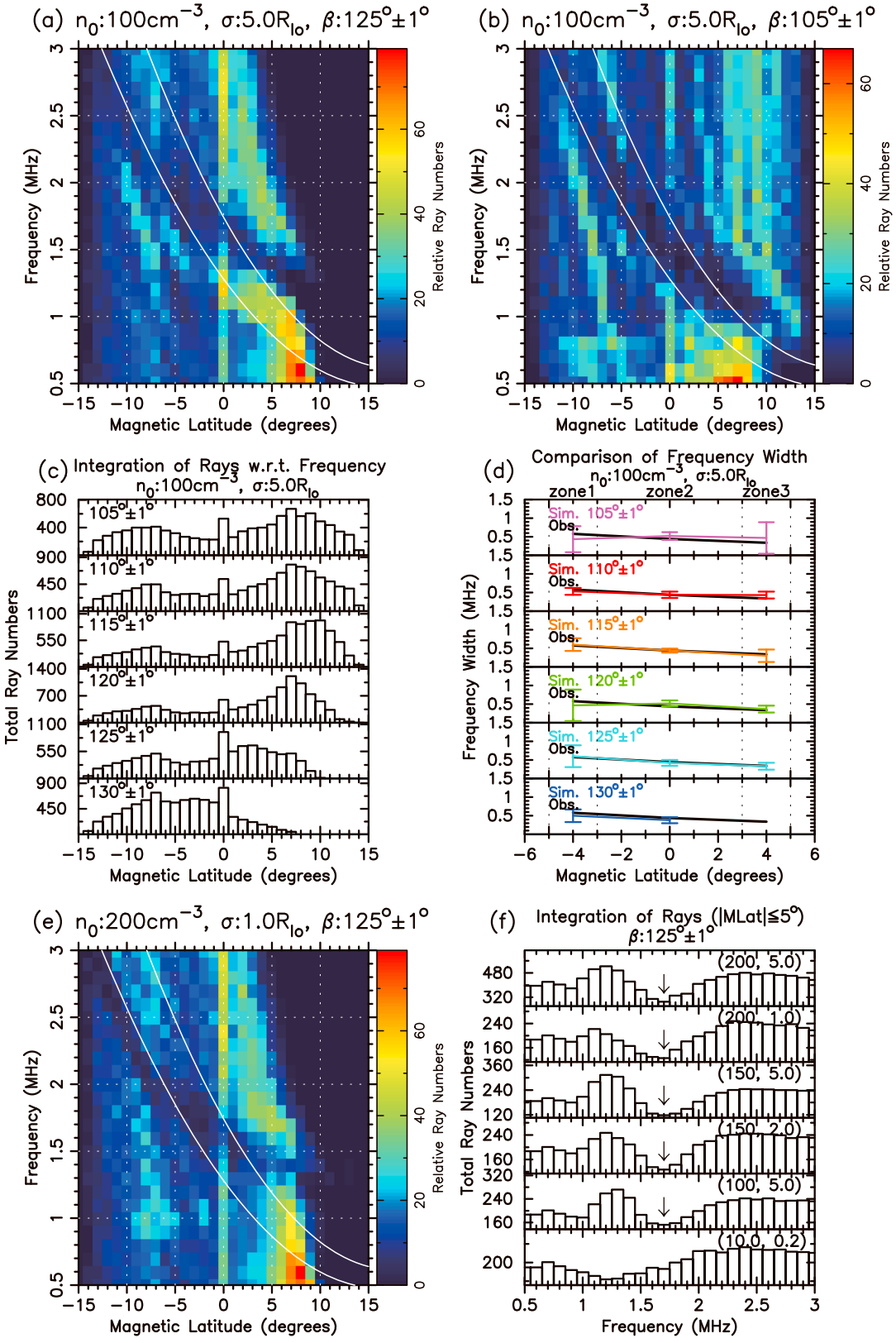

Figure 6. The format is the same as in Figure 4 but for southern hemisphere radio emission.

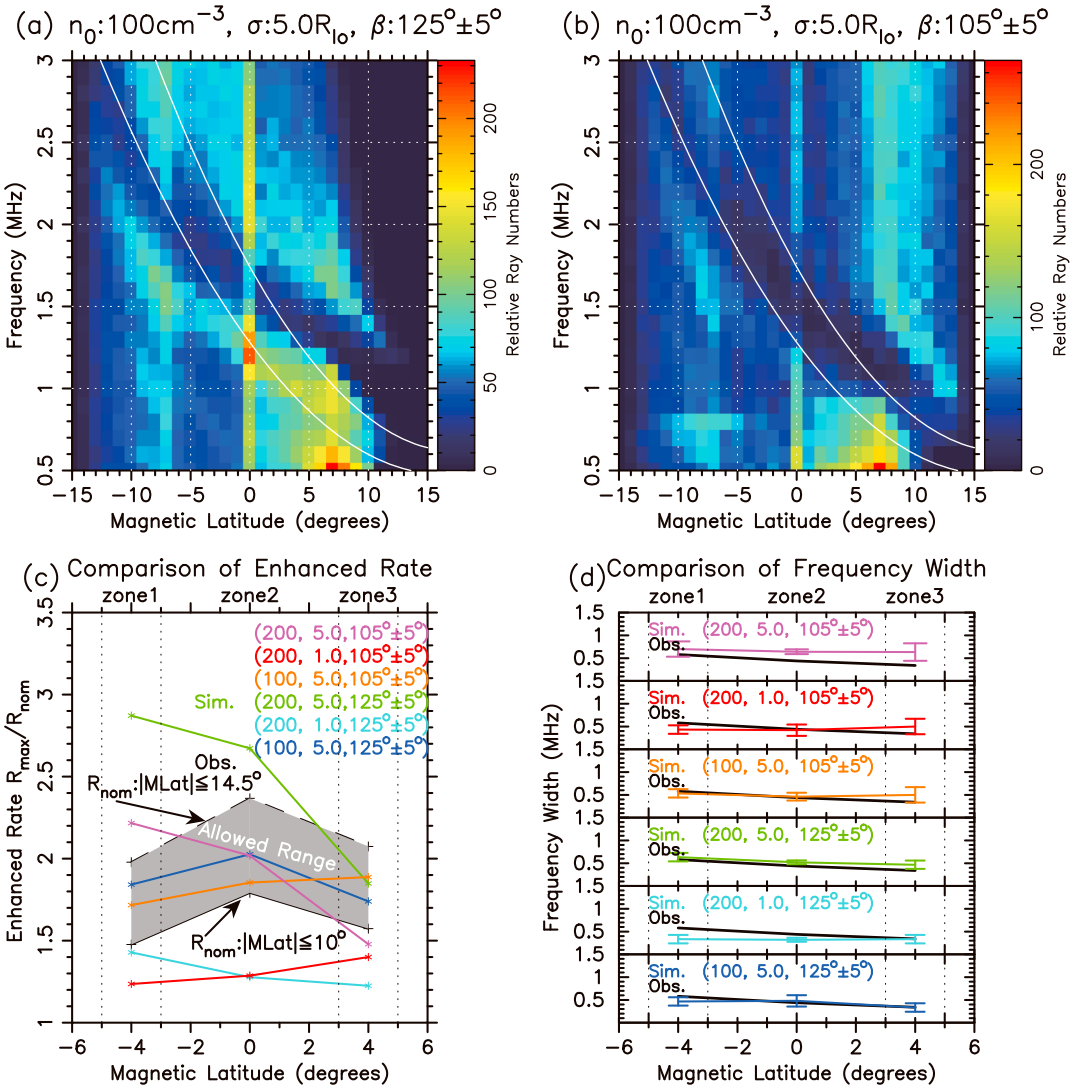

Figure 7. The format is the same as in Figure 5 but for southern hemisphere radio emission.

Figure 7b. On the other hand, the computed attenuation lanes in Figure 7b seems to be a better fit to the white observational curve than in Figure 7a.

In order to inspect the enhanced rate as well as the frequency width of the attenuation lanes, we have plotted two different maps in Figures 7c and 7d. In terms of the enhanced rate, just as in Figure 5c, we have calculated the upper and lower ranges of allowed regions for the Cassini observations based on two different values such as averages of magnetic latitude between −14.5° and +14.5° and between −10° and +10°, respectively. Also, we computed the enhanced rates for the six cases. After considering whether the enhanced rates for ray-tracing computations are fit in the allowed range deduced from the observations, we found that the cases of flux shell density 100 cm^{-3} and breadth 5.0 R_{Io} for both the cone half-angle 125° ± 5° (blue-colored line) and 105° ± 5° (orange-colored line) are appropriate. Concerning the frequency width of the southern attenuation lane, according to the same procedure of Figure 5d, the case of 100 cm^{-3} and breadth 5.0 R_{Io} for the cone half-angle 105° ± 5° (orange-colored line) is the only one that fully satisfies the conditions; the other two cases of (200, 1.0, 105° ± 5°) and (100, 5.0, 125° ± 5°) are partially satisfied.

4. Discussion

The major origin of attenuation lanes has been debated for about three decades and 4 years since their discovery [*Lecacheux et al.*, 1980]. It is thought that the attenuation lanes are due to the ray refraction from

a high-density medium by either Case (i) enhanced density in the magnetic L-shell connected to Io's orbit [*Gurnett et al.*, 1998] or Case (ii) the Io plasma torus itself [*Lecacheux*, 1981]. Recently, *Boudjada et al.* [2011] stated that the magnetic flux shell is "unstable" and not able to support the higher density, thereby being unfavorable for Case (i). Rather, the major contribution results from Case (ii) because the medium may be temporally and spatially stable. However, Case (i) cannot be ruled out because the diffusive equilibrium model [*Moncuquet et al.*, 2002] enables the magnetic flux shell along an *L*-value = 5.7 to retain densities of , say, 60 cm^{-3} and 80 cm^{-3} at 3 R_J and 4 R_J, respectively. Therefore, Case (i) may play a major role in generating the attenuation lanes within Jovian HOM radio emissions.

Our estimation for the enhanced density irregularity is higher than the previous ray-tracing results [*Higgins et al.*, 2001; *Menietti et al.*, 2003]. When we consider the enhanced rate and frequency width of attenuation lanes, the reasonable flux shell model parameters for both hemisphere radio emissions are a maximum density of $n_0 = 100$ cm^{-3} and density breadth of $\sigma = 5.0$ R_{Io}. The total density attained along *L*-value = 5.7 is 160 cm^{-3} for 3 R_J by means of equation (4). *Higgins et al.* [2001] demonstrated simple ray tracing and estimated that a sufficiently enhanced density is approximately 100 cm^{-3}, while *Menietti et al.* [2003], based on a comparison of Cassini and Galileo attenuation lanes with ray-tracing computations, found an allowable range of density from 1 to 10 cm^{-3} and of breadth from 0.088 to 0.44 R_{Io}. The different estimation comes from the background plasma density model dependence as well as the limited radio source setting. In particular, the ray refraction is directly responsible for spatial derivatives of the plasma density, so the background plasma density is a key point in the ray-tracing computations. *Menietti et al.* [2003] removed the plasmasphere model and only added the magnetic flux shell density model, which induces a rapid gradient of plasma density and, in turn, causes HOM rays to veer off course. For this reason, their estimation of plasma density is very small. Our results are different but in reasonable agreement with the work of *Higgins et al.* [2001], who incorporated the plasmasphere model [*Divine and Garrett*, 1983].

The amount of enhanced density irregularity deduced from our study is consistent with that from the *Imai et al.* [1992, 1997] study on modulation lanes within Jovian DAM radio emissions, which are groups of parallel sloping strips of alternately increased and decreased emission intensity in dynamic spectra. *Imai et al.* [1992] proposed a model in which rays emanated from a Jovian DAM radio source toward Earth and pass through a grid-like interference screen, which is composed of field-aligned columns of enhanced plasma density downstream of Io. Radiation traversing the enhanced-plasma columns is more highly scattered than that traversing the lower density regions between columns. Extending the model of *Imai et al.* [1992], *Imai et al.* [1997] computed that the plasma density enhancement within the columns should be ~200 cm^{-3}. This amount of density is comparable to our electron density from the ray-tracing computations of the attenuation lanes.

Our study has verified that all cone half-angles may, overall, produce the attenuation lanes if we have a moderate enhanced density irregularity. In other words, the beaming is not just confined to the particular radio source longitude which is the same CML plane of an observer (demonstrated by *Higgins et al.* [1999, 2001] and *Menietti et al.* [2003]) but also spread to the other radio source longitudes which are away from the plane of the observer but reach the observer in a three-dimensional space. The models show that the frequency width and the enhancement of the attenuation lanes are easily reproduced, but the frequency slopes compared to the observation curves are relatively difficult to model accurately. This may be due to the restriction of the interpolation from a 2-D plasma density model [*Moncuquet et al.*, 2002] to a 3-D one by using the concept of centrifugal axes and axial symmetry. This model is reasonable to represent the average property of the Io plasma torus plasma density but excludes the variations of System III longitude and local time. This effect can be considered only if we incorporate a higher dimensional (i.e., the three spatial dimensions plus local time variations) asymmetrical Io plasma torus model [*Smyth et al.*, 2011]. Nevertheless, in our study, the enhanced rate and the frequency width may not be sensitive to the more sophisticated Io plasma torus model.

The larger cone half-angles tend to agree reasonably well with the observational curves, but the beaming is broad. A likely explanation is that the total number of rays is not necessarily proportional to observed intensity, but instead it is possible that individual rays have different contribution weight to the emissions. In order to handle this problem, tracing a family of neighboring rays plays an important role in computing the physical intensity by means of "enhanced" ray-tracing technique. The physical intensity is defined as the

conservation of the solid angle from radio sources to an observer [*Budden*, 1985]. This is a subject of future study by the authors.

5. Conclusions

We have investigated Jovian attenuation lanes within the HOM radio emissions by using Cassini Jupiter encounter data. For both right- and left-hand polarization responses, the edges of attenuation lanes derived from the statistical results of Cassini data are fitted with a quadratic function by means of the least squares method. Moreover, we have used comprehensive ray-tracing techniques to test the origin of the lanes as refraction from either Case (i) enhanced density in a magnetic flux shell at *L*-value = 5.7 or Case (ii) the Io plasma torus itself or both. The modeling includes a bi-kappa diffusive Io plasma torus model and magnetic flux shell model in addition to Jupiter's global magnetic and plasma models. Our survey assumed emission frequencies of 0.5–3.0 MHz with a cone half-angle β from 40–90° for northern hemisphere radio emission and of 90–130° for southern hemisphere radio emission in the continuous radio source longitudes of polar regions. As a result, our major conclusions from the Cassini data analysis and ray-tracing computations are as follows:

1. The enhanced density in a magnetic flux shell (Case (i)) is better for producing the attenuation lanes than the Io plasma torus itself (Case (ii)) because the interpretation of Case (i) can be accounted for the statistical properties of the attenuation lanes observed by the Cassini spacecraft.
2. The attenuation lanes are seen for all cone half-angles, but the major HOM beaming is confined within $50° \leq \beta \leq 60°$ and $120° \leq \beta \leq 130°$ for northern and southern hemisphere radio emissions, respectively.
3. A reasonable enhanced density is found to be $\sim$100 cm^{-3} with the breadth of the density enhancement across the flux shell, 5.0 Io radii. The total density is the above density plus some specific latitude-dependent density (e.g., between 60 and 80 cm^{-3} for 3 and 4 R_J in the higher latitude along the Io flux shell ribbon region) from the diffusive bi-kappa Io plasma torus model.
4. The ray-tracing computations easily reproduce the frequency widths of the attenuation lanes observed by the Cassini spacecraft by varying the functions of the emitted cone half-angle and flux shell density model parameters (maximum density and breadth). The enhanced rate of the attenuation lanes from ray-tracing results shows that it is sensitive to only the breadth of the magnetic flux shell model.

This enhanced plasma along a magnetic field line may come from Jupiter's ionosphere because the plasmas easily move along the parallel direction of the magnetic field and their characteristics satisfy the quasi-neutral conditions. In our study, the reference densities and temperatures of the diffusive equilibrium model originally were derived from measurements along the trajectory of Voyager 1 at a radial distance of 4 to 12 R_J and a Jovigraphic latitudinal range of −5.9° to −1.2°. They mainly contain the majority of the plasma sources from the Io plasma torus, but, for the higher latitudinal plasmas along the magnetic fields, it is necessary to take into account another source such as the ionosphere. This scenario may suggest a modest constraint on the electron (and proton) density along the magnetic field lines and may, in turn, refine the recent diffusive equilibrium model at Jupiter's inner plasmasphere [*Pierrard*, 2009] in a further study.

Another scenario of the enhanced plasma along a magnetic field line can be accounted for the flexibility of varying the unknown parameters (kappa parameter κ and thermal anisotropy $T_\perp/T_\parallel$) for electrons and ions in the framework of the diffusive equilibrium theory. *Moncuquet et al.* [2002] showed that isotropic kappa distributions of particles tend to sustain higher population at high latitude (see their Figure 3). This suggests that, based on our enhanced plasma at high latitude, an elaborate Io plasma torus model may be developed.

In July 2016, the Juno spacecraft will be the first spacecraft placed in a polar orbit of Jupiter. It will start to monitor the auroras and the magnetosphere in the Jovian system [*Bagenal et al.*, 2014]. Juno has the capability of measuring radio and plasma waves as well as detecting plasma parameters. Also, thanks to the unique polar trajectory, it has a high probability of directly examining a Jovian radio source in situ (in comparison to the cases of Saturnian kilometric radiation by the Cassini spacecraft [*Lamy et al.*, 2010] and terrestrial auroral kilometric radiation by the FAST satellite [*Ergun et al.*, 1998], which are analogous to Jupiter's auroral radio emissions). Juno also has the capability of clearly unveiling any enhanced density irregularities along magnetic field lines just above the auroras and connecting to the Io plasma torus. These new observations will enhance our current understanding of Jupiter's radio emissions as well as the microscopic plasma density profiles around the polar regions.

Acknowledgments
The authors appreciate the referees for fruitful comments with the careful reading of the manuscript. They are also indebted to all members of the Cassini RPWS team, especially to the principal investigators D. A. Gurnett and W. S. Kurth. This work at Kyoto University was supported by a grant-in-aid for Research Fellows of the Japan Society for the Promotion of Science (JSPS). M.I. thanks LESIA of the Observatoire de Paris-Meudon for the generous hospitality during his 1 year visit. Data used for this article are available through request to the authors.

Michael Liemohn thanks the reviewers for their assistance in evaluating this paper.

References

Acuña, M. H., K. W. Behannon, and J. E. P. Connerney (1983), Jupiter's magnetic field and magnetosphere, in *Physics of the Jovian Magnetosphere*, edited by A. J. Dessler, pp. 1–50, Cambridge Univ. Press, New York.

Alexander, J. K., T. D. Carr, J. R. Thieman, J. J. Schauble, and A. C. Riddle (1981), Synoptic observations of Jupiter's radio emissions: Average statistical properties observed by Voyager, *J. Geophys. Res.*, *86*(A10), 8529–8545, doi:10.1029/JA086iA10p08529.

Alexeev, I. I., and E. S. Belenkaya (2005), Modeling of the Jovian magnetosphere, *Ann. Geophys.*, *23*(3), 809–826, doi:10.5194/angeo-23-809-2005.

Bagenal, F. (1994), Empirical model of the Io plasma torus: Voyager measurements, *J. Geophys. Res.*, *99*(A6), 11,043–11,062, doi:10.1029/93JA02908.

Bagenal, F., and P. A. Delamere (2011), Flow of mass and energy in the magnetospheres of Jupiter and Saturn, *J. Geophys. Res.*, *116*, A05209, doi:10.1029/2010JA016294.

Bagenal, F., et al. (2014), Magnetospheric science objectives of the Juno mission, *Space Sci. Rev.*, 1–69, doi:10.1007/s11214-014-0036-8.

Barrow, C., and A. Lecacheux (1995), Problems concerning the radio emission from Jupiter observed by Ulysses after encounter, *Astron. Astrophys.*, *301*, 903–913.

Bigg, E. K. (1964), Influence of the satellite Io on Jupiter's decametric emission, *Nature*, *203*, 1008–1010, doi:10.1038/2031008a0.

Birdsall, C. K., and A. B. Langdon (2005), *Plasma Physics via Computer Simulation, Ser. in Plasma Phys.*, Taylor and Francis, New York.

Birmingham, T. J., J. K. Alexander, M. D. Desch, R. F. Hubbard, and B. M. Pedersen (1981), Observations of electron gyroharmonic waves and the structure of the Io torus, *J. Geophys. Res.*, *86*(A10), 8497–8507, doi:10.1029/JA086iA10p08497.

Boudjada, M., P. H. M. Galopeau, and H. Rucker (2001), Jovian hectometric beam observed by PWS and WAVES experiments on board Galileo and Wind spacecraft, *Planet. Space Sci.*, *49*(10–11), 1151–1158, doi:10.1016/S0032-0633(01)00022-8.

Boudjada, M. Y., P. H. M. Galopeau, H. O. Rucker, A. Lecacheux, N. Mebarki, W. Macher, and W. Voller (2011), Morphological aspects of the attenuation bands associated with Jovian hectometric radiation, *J. Geophys. Res.*, *116*, A11208, doi:10.1029/2010JA016354.

Brown, L. W. (1974), Spectral behavior of Jupiter near 1 MHz, *Astrophys. J.*, *194*, L159–L162, doi:10.1086/181693.

Budden, K. G. (1985), *The Propagation of Radio Waves: The Theory of Radio Waves of Low Power in the Ionosphere and Magnetosphere*, Cambridge Univ. Press, New York.

Carr, T. D., M. D. Desch, and J. K. Alexander (1983), Phenomenology of magnetospheric radio emissions, in *Physics of the Jovian Magnetosphere*, edited by A. J. Dessler, pp. 226–284, Cambridge Univ. Press, New York.

Chapman, S., and J. Bartels (1940), The spherical harmonic analysis of the main field, in *Geomagnetism*, vol. 2, pp. 639–668, Oxford Univ. Press, London.

Clarke, J. T., D. Grodent, S. W. H. Cowley, E. J. Bunce, P. Zarka, J. E. P. Connerney, and T. Satoh (2004), Jupiter's aurora, in *Jupiter: The Planet, Satellites and Magnetosphere*, edited by F. Bagenal, T. E. Dowling, and W. B. McKinnon, chap. 26, pp. 639–670, Cambridge Univ. Press, New York.

Connerney, J. E. P., M. H. Acuña, and N. F. Ness (1981), Modeling the Jovian current sheet and inner magnetosphere, *J. Geophys. Res.*, *86*(A10), 8370–8384, doi:10.1029/JA086iA10p08370.

Connerney, J. E. P., M. H. Acuña, N. F. Ness, and T. Satoh (1998), New models of Jupiter's magnetic field constrained by the Io flux tube footprint, *J. Geophys. Res.*, *103*(A6), 11,929–11,939, doi:10.1029/97JA03726.

Cummings, W., A. Dessler, and T. Hill (1980), Latitudinal oscillations of plasma within the Io torus, *J. Geophys. Res.*, *85*(A5), 2108–2114, doi:10.1029/JA085iA05p02108.

Desch, M. D., and T. D. Carr (1974), Dekametric and hectometric observations of Jupiter from the RAE-1 satellite, *Astrophys. J.*, *194*, L57–L59, doi:10.1086/181667.

Divine, N., and H. B. Garrett (1983), Charged particle distributions in Jupiter's magnetosphere, *J. Geophys. Res.*, *88*(A9), 6889–6903, doi:10.1029/JA088iA09p06889.

Dulk, G. A. (1967), Apparent changes in the rotation rate of Jupiter, *Icarus*, *7*(1–3), 173–182, doi:10.1016/0019-1035(67)90062-0.

Edwards, T., E. Bunce, and S. Cowley (2001), A note on the vector potential of Connerney et al.'s model of the equatorial current sheet in Jupiter's magnetosphere, *Planet. Space Sci.*, *49*(10–11), 1115–1123, doi:10.1016/S0032-0633(00)00164-1.

Engle, I. M. (1991), Idealized Voyager Jovian magnetosphere shape and field, *J. Geophys. Res.*, *96*(A5), 7793–7802, doi:10.1029/90JA02391.

Engle, I. M. (1992), Diurnal variation in Jovian subsolar magnetopause position, *J. Geophys. Res.*, *97*(A11), 17,169–17,172, doi:10.1029/92JA02036.

Ergun, R. E., et al. (1998), FAST satellite wave observations in the AKR source region, *Geophys. Res. Lett.*, *25*(12), 2061–2064, doi:10.1029/98GL00570.

Fischer, G., W. Macher, H. O. Rucker, H. P. Ladreiter, D. F. Vogl, and the Cassini/RPWS Team (2001), Wire-grid modeling of Cassini spacecraft for the determination of effective antenna length vectors of the RPWS antennas, in *Planetary Radio Emissions V*, edited by H. O. Rucker, M. L. Kaiser, and Y. Leblanc, pp. 347–356, Austrian Acad. Sci., Vienna.

Fung, S. F., and J. L. Green (2005), Modeling of field-aligned guided echoes in the plasmasphere, *J. Geophys. Res.*, *110*, A01210, doi:10.1029/2004JA010658.

Green, J. L. (1984), The Io decametric emission cone, *Radio Sci.*, *19*(2), 556–570, doi:10.1029/RS019i002p00556.

Green, J. L. (1988), Ray tracing planetary radio emissions, in *Planetary Radio Emissions II*, edited by H. O. Rucker, S. J. Bauer, and B. M. Pedersen, pp. 343–368, Austrian Acad. Sci., Vienna.

Green, J. L., J. R. Thieman, C. Higgins, S. F. Fung, R. M. Candey, and L. Aist-Sagara (1992), Lane features in Jovian hectometric radio emissions, in *Planetary Radio Emissions III*, edited by H. O. Rucker, S. J. Bauer, and B. M. Pedersen, pp. 91–104, Austrian Acad. Sci., Vienna.

Gurnett, D., et al. (2004), The Cassini radio and plasma wave investigation, *Space Sci. Rev.*, *114*(1–4), 395–463, doi:10.1007/s11214-004-1434-0.

Gurnett, D. A., W. S. Kurth, J. D. Menietti, and A. M. Persoon (1998), An unusual rotationally modulated attenuation band in the Jovian hectometric radio emission spectrum, *Geophys. Res. Lett.*, *25*(11), 1841–1844, doi:10.1029/98GL01400.

Gurnett, D. A., et al. (2002), Control of Jupiter's radio emission and aurorae by the solar wind, *Nature*, *415*, 985–987, doi:10.1038/415985a.

Haselgrove, J. (1955), Ray theory and a new method for ray tracing, in *Report of Conference on the Physics of the Ionosphere*, edited by A. C. Stickland, pp. 355–364, Phys. Soc., London.

Hashimoto, K., and M. L. Goldstein (1983), A theory of the Io phase asymmetry of the Jovian decametric radiation, *J. Geophys. Res.*, *88*(A3), 2010–2020, doi:10.1029/JA088iA03p02010.

Hess, S., B. Cecconi, and P. Zarka (2008), Modeling of Io-Jupiter decameter arcs, emission beaming and energy source, *Geophys. Res. Lett.*, *35*, L13107, doi:10.1029/2008GL033656.

Hess, S., A. Pétin, P. Zarka, B. Bonfond, and B. Cecconi (2010), Lead angles and emitting electron energies of Io-controlled decameter radio arcs, *Planet. Space Sci.*, *58*(10), 1188–1198, doi:10.1016/j.pss.2010.04.011.

Hess, S. L. G., B. Bonfond, P. Zarka, and D. Grodent (2011), Model of the Jovian magnetic field topology constrained by the Io auroral emissions, *J. Geophys. Res.*, *116*, A05217, doi:10.1029/2010JA016262.

Higgins, C. A., J. L. Green, J. R. Thieman, S. F. Fung, and R. M. Candey (1995), Structure within Jovian hectometric radiation, *J. Geophys. Res.*, *100*(A10), 19,487–19,496, doi:10.1029/95JA01128.

Higgins, C. A., J. R. Thieman, S. F. Fung, J. L. Green, and R. M. Candey (1998), Latitudinal structure within Jovian hectometric radiation, *J. Geophys. Res.*, *103*(A11), 26,679–26,686, doi:10.1029/98JA02393.

Higgins, C. A., J. R. Thieman, S. F. Fung, J. L. Green, and R. M. Candey (1999), Jovian dual-sinusoidal HOM lane features observed by Galileo, *Geophys. Res. Lett.*, *26*(3), 389–392, doi:10.1029/1998GL900302.

Higgins, C. A., J. R. Thieman, S. F. Fung, J. L. Green, and R. M. Candey (2001), Simple ray tracing of Galileo-observed hectometric attenuation features, *Radio Sci.*, *36*(6), 1713–1721, doi:10.1029/2000RS002457.

Hill, T. W., A. J. Dessler, and F. C. Michel (1974), Configuration of the Jovian magnetosphere, *Geophys. Res. Lett.*, *1*(1), 3–6, doi:10.1029/GL001i001p00003.

Imai, K., L. Wang, and T. D. Carr (1992), A model for the production of Jupiter's decametric modulation lanes, *Geophys. Res. Lett.*, *19*(9), 953–956, doi:10.1029/92GL00942.

Imai, K., L. Wang, and T. D. Carr (1997), Modeling Jupiter's decametric modulation lanes, *J. Geophys. Res.*, *102*(A4), 7127–7136, doi:10.1029/96JA03960.

Imai, M., K. Imai, C. A. Higgins, and J. R. Thieman (2008), Angular beaming model of Jupiter's decametric radio emissions based on Cassini RPWS data analysis, *Geophys. Res. Lett.*, *35*, L17103, doi:10.1029/2008GL034987.

Imai, M., K. Imai, C. A. Higgins, and J. R. Thieman (2011a), Comparison between Cassini and Voyager observations of Jupiter's decametric and hectometric radio emissions, *J. Geophys. Res.*, *116*, A12233, doi:10.1029/2011JA016456.

Imai, M., A. Lecacheux, K. Imai, C. A. Higgins, and J. R. Thieman (2011b), Jupiter's decametric and hectometric radio emissions observed by Cassini RPWS and Voyager PRA, in *Planetary Radio Emissions VII*, edited by H. O. Rucker et al., pp. 167–176, Vienna, Austrian Acad. Sci., doi:10.1553/PRE7s167.

Khurana, K. K. (1997), Euler potential models of Jupiter's magnetospheric field, *J. Geophys. Res.*, *102*(A6), 11,295–11,306, doi:10.1029/97JA00563.

Khurana, K. K., and H. K. Schwarzl (2005), Global structure of Jupiter's magnetospheric current sheet, *J. Geophys. Res.*, *110*, A07227, doi:10.1029/2004JA010757.

Kimura, I. (1966), Effects of ions on whistler-mode ray tracing, *Radio Sci.*, *1*, 269–283.

Kimura, I. (1997), Ray tracing technique applied to ELF and VLF wave propagation in the magnetosphere, in *Discovery of the Magnetosphere*, vol. 7, edited by C. S. Gillmor and J. R. Spreiter, pp. 119–128, AGU, Washington, D. C., doi:10.1029/HG007p0119.

Kimura, T., F. Tsuchiya, H. Misawa, A. Morioka, and H. Nozawa (2008), Occurrence and source characteristics of the high-latitude components of Jovian broadband kilometric radiation, *Planet. Space Sci.*, *56*(8), 1155–1168, doi:10.1016/j.pss.2008.03.001.

Kurth, W. S., S. J. Bolton, D. A. Gurnett, and S. Levin (1997), A determination of the source of Jovian hectometric radiation via occultation by Ganymede, *Geophys. Res. Lett.*, *24*(10), 1171–1174, doi:10.1029/97GL00988.

Ladreiter, H., P. Zarka, and A. Lecacheux (1994), Direction finding study of Jovian hectometric and broadband kilometric radio emissions: Evidence for their auroral origin, *Planet. Space Sci.*, *42*(11), 919–931, doi:10.1016/0032-0633(94)90052-3.

Ladreiter, H. P., and Y. Leblanc (1990a), Source location of the Jovian hectometric radiation via ray-tracing technique, *J. Geophys. Res.*, *95*(A5), 6423–6435, doi:10.1029/JA095iA05p06423.

Ladreiter, H. P., and Y. Leblanc (1990b), Modeling of the Jovian hectometric radiation: A three-dimensional study, *Ann. Geophys.*, *8*(7–8), 477–488.

Ladreiter, H. P., and Y. Leblanc (1991a), The Jovian hectometric radiation: An overview after the Voyager mission, *Ann. Geophys.*, *9*, 784–796.

Ladreiter, H. P., and Y. Leblanc (1991b), Prediction of the Ulysses Jovian hectometric observations, *J. Geophys. Res.*, *96*(A12), 21,207–21,212, doi:10.1029/91JA02265.

Lamy, L., et al. (2010), Properties of Saturn kilometric radiation measured within its source region, *Geophys. Res. Lett.*, *37*, L12104, doi:10.1029/2010GL043415.

Lecacheux, A. (1978), Direction finding of a radiosource of unknown polarization with short electric antennas on a spacecraft, *Astron. Astrophys.*, *70*, 701–706.

Lecacheux, A. (1981), Ray tracing in the Io plasma torus: Application to the PRA observations during Voyager 1's closest approach, *J. Geophys. Res.*, *86*(A10), 8523–8528, doi:10.1029/JA086iA10p08523.

Lecacheux, A. (2011), Direction finding and polarization measurements of SKR, in *Planetary Radio Emissions VII*, edited by H. O. Rucker et al., pp. 13–36, Austrian Acad. Sci., Vienna, doi:10.1553/PRE7s13.

Lecacheux, A., B. Moller-Pedersen, A. C. Riddle, J. B. Pearce, A. Boischot, and J. W. Warwick (1980), Some spectral characteristics of the hectometric Jovian emission, *J. Geophys. Res.*, *85*(A12), 6877–6882, doi:10.1029/JA085iA12p06877.

Macher, W. (2008), Transfer matrix description of multi-port antennas and its application to the Mars Express/MARSIS radar, PhD thesis, Graz Univ. of Technol., Graz, Austria.

Menietti, J., D. Gurnett, G. Hospodarsky, C. Higgins, W. Kurth, and P. Zarka (2003), Modeling radio emission attenuation lanes observed by the Galileo and Cassini spacecraft, *Planet. Space Sci.*, *51*(9–10), 533–540, doi:10.1016/S0032-0633(03)00078-3.

Menietti, J. D., and M. J. Reiner (1996), Modeling of Jovian hectometric radiation source locations: Ulysses observations, *J. Geophys. Res.*, *101*(A12), 27,045–27,052, doi:10.1029/96JA02403.

Menietti, J. D., J. L. Green, S. Gulkis, and F. Six (1984a), Three-dimensional ray tracing of the Jovian magnetosphere in the low-frequency range, *J. Geophys. Res.*, *89*(A3), 1489–1495, doi:10.1029/JA089iA03p01489.

Menietti, J. D., J. L. Green, S. Gulkis, and N. F. Six (1984b), Jovian decametric arcs: An estimate of the required wave normal angles from three-dimensional ray tracing, *J. Geophys. Res.*, *89*(A10), 9089–9094, doi:10.1029/JA089iA10p09089.

Menietti, J. D., D. A. Gurnett, W. S. Kurth, and J. B. Groene (1999), Effectiveness of near-grazing incidence reflection in creating the rotationally modulated lanes in the Jovian hectometric radio emission spectrum, *Radio Sci.*, *34*(4), 1005–1012, doi:10.1029/1999RS900036.

Menietti, J. D., D. A. Gurnett, J. R. Spencer, and J. A. Stansberry (2001), Relationship between Jovian hectometric attenuation lanes and Io volcanic activity, *Radio Sci.*, *36*(6), 1723–1731, doi:10.1029/2000RS002458.

Moncuquet, M., F. Bagenal, and N. Meyer-Vernet (2002), Latitudinal structure of outer Io plasma torus, *J. Geophys. Res.*, *107*(A9), 1260, doi:10.1029/2001JA900124.

Ortega-Molina, A., and A. Lecacheux (1991), Polarization of Jovian hectometric emission, *J. Geophys. Res.*, *96*(A7), 11,441–11,453, doi:10.1029/90JA00103.
Pierrard, V. (2009), Kinetic models for the exospheres of Jupiter and Saturn, *Planet. Space Sci.*, *57*(11), 1260–1267, doi:10.1016/j.pss.2009.04.011.
Ralston, A. (1960), Numerical integration methods for the solution of ordinary differential equations, in *Mathematical Methods for Digital Computers*, edited by A. Ralston and H. S. Wilf, chap. 8, pp. 95–109, John Wiley, New York.
Reiner, M. J., J. Fainberg, and R. G. Stone (1993), Source characteristics of Jovian hectometric radio emissions, *J. Geophys. Res.*, *98*(E10), 18,767–18,777, doi:10.1029/93JE01779.
Rief, G. (2013), Numerical calibration of the Cassini RPWS antenna system, Master's thesis, Karl-Franzens-Universität Graz, Graz, Austria.
Riihimaa, J. J. (1968), Structured events in the dynamic spectra of Jupiter's decametric radio emission, *Astron. J.*, *73*, 265–270, doi:10.1086/110627.
Schneider, N. M., and J. T. Trauger (1995), The structure of the Io torus, *Astron. J.*, *450*, 450–462, doi:10.1086/176155.
Smith, E. J., L. Davis Jr., and D. E. Jones (1976), Jupiter's magnetic field and magnetosphere, in *Jupiter*, edited by T. Gehrels, pp. 788–829, Univ. of Ariz. Press, Tucson.
Smyth, W. H., C. A. Peterson, and M. L. Marconi (2011), A consistent understanding of the ribbon structure for the Io plasma torus at the Voyager 1, 1991 ground-based, and Galileo J0 epochs, *J. Geophys. Res.*, *116*, A07205, doi:10.1029/2010JA016094.
Stix, T. H. (1992), *Waves in Plasmas*, Springer, New York.
Thomas, N., F. Bagenal, T. W. Hill, and J. K. Wilson (2004), The Io neutral clouds and plasma torus, in *Jupiter: The Planet, Satellites and Magnetosphere*, edited by F. Bagenal, T. E. Dowling, and W. B. McKinnon, chap. 23, pp. 561–591, Cambridge Univ. Press, New York.
Treumann, R. A. (2006), The electron-cyclotron maser for astrophysical application, *Astron. Astrophys. Rev.*, *13*(4), 229–315, doi:10.1007/s00159-006-0001-y.
Vogl, D. F., et al. (2004), In-flight calibration of the Cassini-Radio and Plasma Wave Science (RPWS) antenna system for direction-finding and polarization measurements, *J. Geophys. Res.*, *109*, *A9*, A09S17, doi:10.1029/2003JA010261.
Vogt, M. F., M. G. Kivelson, K. K. Khurana, R. J. Walker, B. Bonfond, D. Grodent, and A. Radioti (2011), Improved mapping of Jupiter's auroral features to magnetospheric sources, *J. Geophys. Res.*, *116*, A03220, doi:10.1029/2010JA016148.
Wu, C. S., and L. C. Lee (1979), A theory of the terrestrial kilometric radiation, *Astrophys. J.*, *230*, 621–626, doi:10.1086/157120.
Yabroff, I. (1961), Computation of whistler ray paths, *J. Res. Nat. Bur. Stand.*, *65D*, 485–505, doi:10.6028/jres.065D.061.
Zarka, P. (1998), Auroral radio emissions at the outer planets: Observations and theories, *J. Geophys. Res.*, *103*(E9), 20,159–20,194, doi:10.1029/98JE01323.